Earthquake rupture dependence on hypocentral location along the Nicoya Peninsula subduction megathrust

Hongfeng Yang[*1], Suli Yao[1], Bing He[1], and Andrew Newman[2]

[1] Earth System Science Programme, The Chinese University of Hong Kong, Shatin, Hong Kong, China

[2] School of Earth and Atmospheric Sciences, Georgia Institute of Technology, Atlanta, GA, USA

[*]Corresponding author (hyang@cuhk.edu.hk)

Abstract

Although interseismic locking distributions have been used in qualitatively evaluating the future earthquake potential, quantitatively estimating how an earthquake may rupture through the locked interface is a more useful tool for quantifying both seismic and tsunami hazards. Here, we investigate rupture scenarios from interseismic locking models along the megathrust interface below Nicoya peninsula, Costa Rica using spontaneous rupture simulations. We first estimate initial stress from locking, then initiate spontaneous ruptures at different nucleation points and observe the eventual earthquake magnitudes and slip distribution. We find that ~40% of nucleations tested develop into large earthquakes of Mw>7.2 based on present interseismic locking models. Of these events, those nucleated from deeper depths have a tendency for larger-amplitude shallow slip, suggesting increased tsunami potential. Furthermore, irrespective of the input locking models we do not observe rupture scenarios of earthquakes with intermediate magnitudes between 6 and 7, a result consistent with observations in Nicoya. The results of hypocentre-dependent earthquake magnitudes and tsunamigenic potential not only pose challenges in estimating rupture extents from locking models, but also underscore the significance of quantitatively evaluating seismic and tsunami hazard in subduction zones.

1. Introduction

In past decade, interseismic locking distribution derived from geodetic studies has significantly improved our understanding of a future earthquake's potential, in particular at subduction zones where great earthquakes occur, sometimes causing devastating tsunami (e.g. *Moreno et al.*, 2010; *Wang et al.*, 2012; *McCaffrey et al.*, 2013). However, considerable uncertainties exist in such interseismic locking models depending on different material rheology properties, subduction fault geometry, and dataset that are used to constrain the locking. One fundamental limit comes from the fact that the locked-then-ruptured megathrust interface resides almost exclusively offshore in subduction zone environments, with limited constraints from inland observations. A typical example is the Cascadia subduction zone where dense on-land geodetic networks are available. Although it is believed the Cascadia megathrust is locked, the present locking models show considerable controversies in the locking degree and downdip spatial extent along Central Oregon (*Burgette et al.*, 2009; *McCaffrey et al.*, 2013; *Schmalzle et al.*, 2014; *Pollitz and Evans*, 2017; *Li et al.*, 2018). Even for a subduction environment such as the Nicoya Peninsula of Costa Rica, where the locked-then-ruptured patch is almost entirely located under land, different locking models have been obtained using different datasets and megathrust geometry (*Feng et al.*, 2012; *Xue et al.*, 2015; *Kyriakopoulos and Newman*, 2016). Thus, it remains unclear how to infer future earthquake sizes from the locking models.

Quantitative evaluations of future rupture scenarios from interseismic locking distributions were performed in a few subduction zones. For instance, *Hok et al.* (2011) developed dynamic rupture scenarios of anticipated Nankai-Tonankai earthquakes, southwest Japan using a boundary integral method. They concluded that rupture segmentation was associated with the prescribed along-strike variation of fracture energy. Because we do not know when the next Nankai-Tonankai earthquake will occur, we cannot yet compare the numerical rupture scenarios with field observations recorded by modern instruments. More recently, *Yang et al.* (2019) derived rupture scenarios from locking models in the Nicoya Peninsula, Central America, and then validated the numerical results with kinematic source models of the 2012 M_w 7.6 Nicoya earthquake, which occurred directly under the peninsula. The rupture was initiated at the hypocentre of the 2012 Nicoya earthquake and spontaneously propagated on the fault plane (*Yang et al.*, 2019). The final moment magnitude, coseismic slip distribution, and moment rate function are well consistent with those kinematic solutions (*Yue et al.*, 2013), demonstrating that, for the first time, deriving a reasonable approximation of the coseismic slip distribution and rupture process from interseismic locking is feasible (*Yang et al.*, 2019).

Although it seems possible to derive reliable rupture scenarios (*Yang et al.*, 2019), it is critical that such a model also accurately describes rupture nucleation from the hypocentre of the 2012 Nicoya earthquake. Indeed, we do not know where future earthquakes may nucleate (*Lapusta and Rice*, 2003; *Hori et al.*, 2004), owing to our limited understanding of loading and the heterogeneous distribution of stress and fault strength. Even after the occurrence of an earthquake, e.g. the 2012 Nicoya earthquake, hypocentre bears uncertainties depending on data used and method of determination (*Quintero et al.*, 2014; *Yue et al.*, 2013). For example, the hypocentre used to derive kinematic source process in *Yue et al.* (2013) corresponds to a low stress environment in both locking models (*Feng et al.*, 2012; *Xue et al.* 2015). Because we do not know where future earthquakes may nucleate solely based on locking models, we investigate the effects of nucleation positions on coseismic rupture scenarios.

In this study, we conduct spontaneous rupture simulations based on interseismic locking models by considering a range of hypocentral locations. Our geographical focus is the Nicoya Peninsula because it protrudes seaward, forming a unique environment allowing near-field inland geodetic observations directly above one of the locked patches (Figure 1). As such, the

80　locking models in the region bear much less uncertainties than those in other subduction zones.
81　We will derive hypocentral dependent rupture scenarios from two late-interseismic locking
82　models that were derived along the same curviplanar megathrust geometry, one building on
83　trench-normal and vertical GPS from 1996 to 2010 (*Feng et al.*, 2012) while the other one also
84　incorporating trench-parallel GPS and line-of-site Interferometric Synthetic Aperture Radar
85　(InSAR) data from 2007 to 2011 that may have improved some resolution of features (*Xue et*
86　*al.*, 2015). Even with the most precise and dense land-based geodetic data, offshore
87　resolvability of megathrust interface features drop-off rapidly, and the ability to recover
88　substantial locking or slip information more than 20 km offshore is negligible (*Williamson and*
89　*Newman*, 2018). Fore-knowledge of such limitations was one of the reasons that Nicoya was
90　chosen for continued study, because the location of the peninsula places the locking and
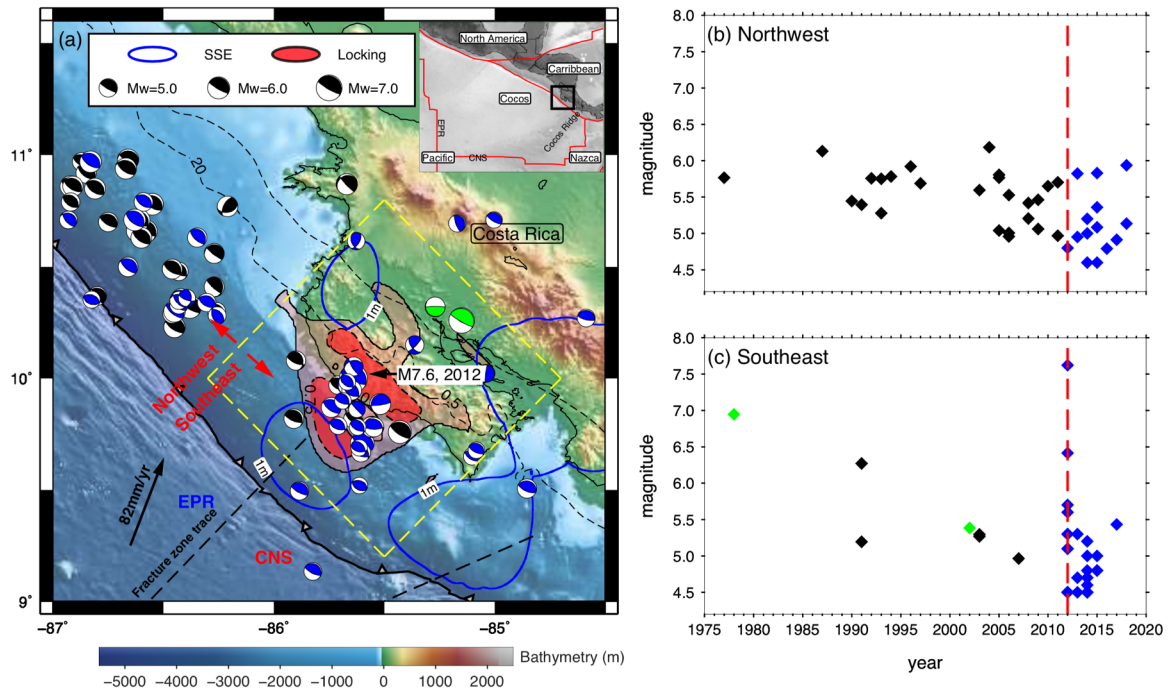91　seismogenic slip region directly under land, and available for detailed analysis.

Figure 1: (a) (inset) Tectonic setting of the Nicoya Peninsula. The interseismic locking contours (locking degrees of 0.75 and 0.5) and moment tensor solutions of interface earthquakes in the region. Colours of beach balls show occurrence time before (black: GCMT) and after (blue: GCMT and *Chaves et al.*, 2017) the 2012 mainshock, as well as inland locations (green). Areas with slow slip events are shown in blue polygons, which represent 1 m of accumulative slip. Thin dashed lines show slab top depth contours of 20 and 40 km (*Kyriakopoulos* et al., 2015), respectively. EPR: East Pacific Rise; CNS: Cocos-Nazca spreading center. (b) Magnitude and occurrence time of interface earthquakes northwest to (b) and beneath the peninsula (c). Colours correspond to the beach balls in panel (a).

92

93　**2.　Method and model set up**
94　　　　Here we conduct spontaneous rupture simulations using a finite element package, Pylith
95　(*Aagaard et al.*, 2013). A number of ingredients to simulating dynamic ruptures play critical
96　roles in the results, including fault geometry and material properties, as well as appropriately
97　estimating the initial stress distribution and constitutive parameters. A smoothly curved fault
98　geometry that was used to invert for the locking models (*Feng et al.*, 2012; *Xue et al.*, 2015) is
99　used to generate the mesh. The fault model created by Feng and later used by Xue was created
100　from a central 2D transect of 3D relocated microseismicity within the central Nicoya Peninsula
101　(see Feng et al. 2012), corresponding to the central locked region. This model remains a good
102　approximation for the northern portion of Nicoya, however southern Nicoya does have a

103 higher-standing plateau as later clearly observed in Kyriakopoulos et al. (2015). As shown in
104 *Yang et al.*, (2019), rupture scenarios in the Nicoya region appear to be independent on material
105 properties. Therefore, we incorporate a half space material property in our domain, which
106 extends 180 km along-strike, 170 km perpendicular to strike, and 80 km at depth. All
107 boundaries except for the free surface are set as absorbing boundaries to avoid energy reflected
108 from the boundary surfaces.
109   The fault is governed by the linear slip-weakening law (*Ida*, 1972). Effective normal
110 stress, $\bar{\sigma} = \sigma - p$, is the difference between normal stress σ and pore-pressure p. The pore-
111 pressure in subduction zones is suggested to be close to lithostatic at the up-dip and down-dip
112 ends of the seismogenic zone (*Saffer and Tobin*, 2011). Therefore, effective normal stress can
113 be approximated by a constant as discussed by *Rice* (1992). For simplicity, the effective normal
114 stress is taken as 50 MPa, as is commonly used in previous studies (e.g., *Yang et al.*, 2012;
115 *Weng and Yang*, 2017). The critical slip distance is taken as a spatially uniform constant, 0.4
116 m, consistent with the average value of the 2012 Nicoya earthquake that was estimated from
117 near-field observations (*Yao and Yang*, 2018).
118   To estimate the initial stress distribution, it is critical to create a sufficiently good slip
119 deficit and rupture history approximation. Here, we follow the approach adopted in *Yang et al.*
120 (2019). Our primary limitation is that we assume that immediately after the prior earthquake,
121 the fault locks up, and that the features we saw in the late intereseismic are the same as they
122 were just after the last event. With this assumption, the slip deficit can be summed as the linear
123 accumulation of stress build-up between events. This assumption is reasonable in the Nicoya
124 region, because nearly no interface earthquakes with magnitudes larger than 6 occurred in the
125 locked region between the more characteristic M_W 7.5+ megathrust events (Figure 1). Thrust
126 earthquakes with moment magnitudes larger than 5 are also limited according to the GCMT
127 catalogue (Figure 1), indicating very little seismic release of the slip deficit on the megathrust.
128 Moreover, detected slow slip events (SSEs) in the region have very small spatial overlaps with
129 the locked patches (*Dixon et al.*, 2014). If the overlapped region did slip in slow slip events
130 before the 2012 M_w 7.6 earthquake, our slip deficit will be slightly overestimated because SSEs
131 usually slip in centimetres in an individual event. Thus, the potential effects of SSEs on slip
132 deficit in the locking regions are minimal and would not significantly affect our results.
133 Furthermore, we test potential impact of uncertainties in slip deficit on our rupture scenarios
134 by considering a backslip rate 11 mm/yr higher than the plate convergence rate (82 mm/yr).
135 The moment magnitudes and final slip distribution derived from both locking models are not
136 significantly affected (Figure S1), reassuring that uncertainties in the amplitude of the slip
137 deficit play little roles in our results.
138   We next assume that the accumulated slip deficit will be completely released by a large
139 (M>7) earthquake because we aim at evaluating the worst scenario. Thus the slip deficit is used
140 to calculate the static stress drop of the earthquake. Since the last M_W 7.5+ 1950 earthquake,
141 the stress build-up $\Delta\tau$ is calculated from the slip deficit for 62 years (1950-2012). The initial
142 stress τ_0 is then calculated from the stress drop and a constant dynamic friction coefficient
143 (*Weng and Yang*, 2018; *Yang et al.*, 2019), showing a heterogeneous distribution corresponding
144 to the locking models (Figure 2a&d). High stress regions generally correlate with patches of
145 high locking degrees (>0.75) because the variation in locking degrees is rather smooth in the
146 two locking models. However, the highest stress regions appear to locate near the edge of the
147 down-dip locked patch (Figure 2a&d), where the locking gradient is the largest. Fault strength
148 τ_s is assumed to be spatially uniform and is set to be slightly larger than the maximum initial
149 stress (*Yang et al.*, 2019). Because the locking models are regularized by smoothing
150 parameters, generally that minimize the second-order derivative of slip (first-order derivative
151 of strain or stress), and a selective choice is made that will control the resultant fault stress field,
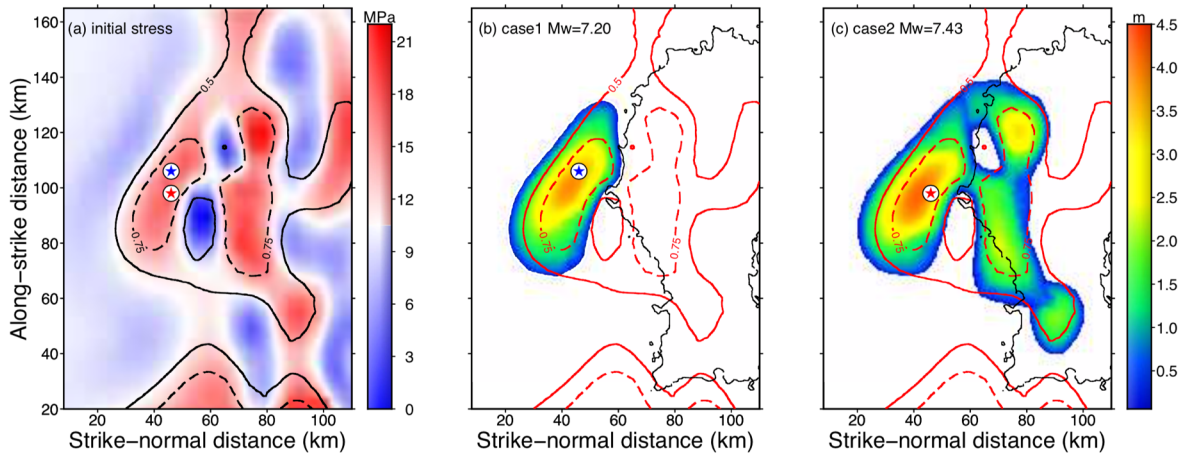152 the fields derived here should be considered in a relative sense.

Figure 2: (a) Initial stress distribution that is derived from interseismic locking distribution (*Xue et al.*, 2015). Blue and red stars denote two nucleation zones at the same depth, having identical initial stresses and sizes (3 km). (b) and (c), Slip distribution of scenario earthquakes that were initiated from the blue (b) and red (c) stars. Solid and dashed lines show the locking model. (d), (e), and (f) are same to (a), (b), and (c) panels, respectively, except these are for the Feng locking model (*Feng et al.*, 2012).

3. Effect of nucleation zone locations on coseismic ruptures

Given the heterogeneous stress distribution, the rupture is expected to nucleate from the high stress regions subject to tectonic loading at greater depths. However, the SSEs surrounding the locked patches may potentially promote coseismic ruptures initiating from the shallow region (Figure 1). Indeed, seven SSEs were identified in the Nicoya region from April 2007 to April 2012, with irregular interval (4-16 months) and summed slip comparable to that of the 2012 Nicoya earthquake but in a much more expanded area (*Dixon et al.*, 2014). Furthermore, although it is not quantified, heterogeneous strength distribution on the megathrust is implied by seismic studies (*Audet and Schwartz*, 2013; *Chaves and Schwartz*, 2016), and thus the rupture may start from any location in the locking region. Therefore, we divide the locking region into an 8 by 9 grid and nucleate the rupture in each node (Figure 3a) to observe the eventual rupture scenarios.

Since we focus on the coseismic process, we artificially nucleate ruptures in a circular patch by decreasing the strength 0.01 MPa lower than the average initial stress to avoid non-uniform stress excess at different locations. We also ensure a reasonable rupture speed (<0.8 Vs) within the nucleation zone to minimize the artificial nucleation effects (*Bizzarri*, 2010). It has been discussed in details how the sizes of nucleation zones vary in different locations given a heterogeneous stress distribution (*Ripperger et al.*, 2007; *Yang et al.*, 2019). Here we adopt a few circular radii (i.e. 3, 4, and 5 km) as the nucleation sizes. We consider 5 km as our upper limit because it corresponds to the typical rupture dimension of an M6 earthquake (~10 km). Consequently, rupture scenarios with magnitudes less than 5 should be ignored because of our lower limit on the nucleation size.

The resultant 216 rupture scenarios are dependent on the location of nucleation within the grid due to the heterogeneous stress distribution. Even for two ruptures that started in neighbouring locations at the same depth with nearly identical initial stress level, the eventual slip distributions and earthquake magnitudes are distinctly different (Figure 2). For instance, the rupture nucleated relatively north (blue star in Figure 2a) within the high locking area (>0.75) in the Xue locking model only breaks the updip locked patch, forming an M_w 7.2 earthquake (Figure 2b). In contrast, the rupture initiated next to it (red star in Figure 2a) has successfully propagated into the downdip locked patch and ends with an M_w 7.4 earthquake, twice of the moment released by the former one (Figure 2c). In addition, the slip distribution

185 exhibits appreciable heterogeneity (Figure 2) in the downdip high locking region (>0.75). Such
186 pattern also holds true for the Feng locking model, in which one rupture nearly broke the entire
187 locked patches (Figure 2e) while the other one nucleating from the neighbouring location did
188 not propagate far from the hypocentre (Figure 2f), highlighting the dominant effects of
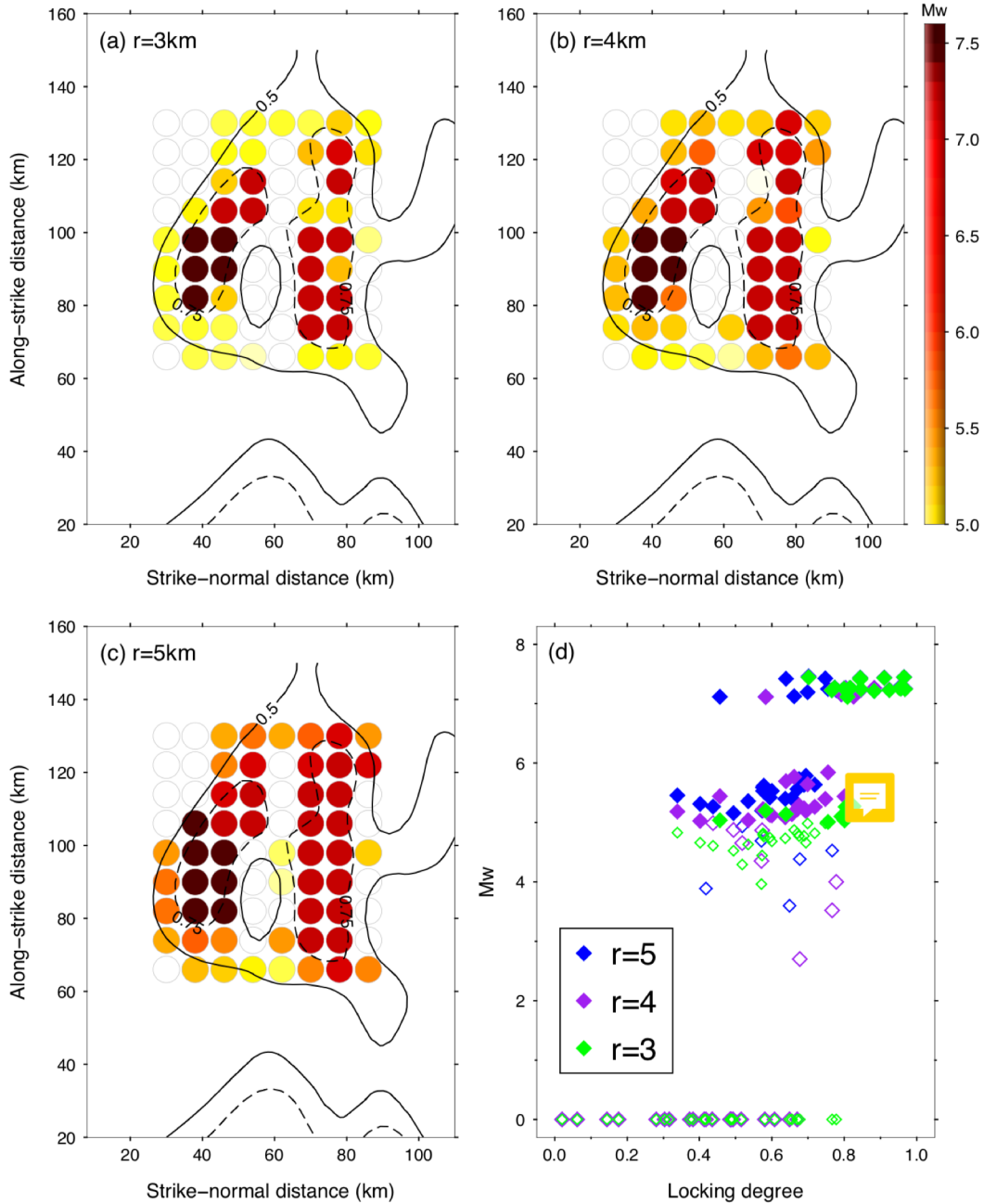189 heterogeneous stress on rupture propagation.

Figure 3: (a), (b), and (c) Map view of the locking degree (contours) and moment magnitudes of rupture scenarios nucleated at each location (circles). Each panel shows the results of different nucleation sizes (3, 4, and 5 km). (d) Relationship between the locking degree and moment magnitudes of location-dependent rupture scenarios, with colours representing different nucleation sizes (3, 4, and 5 km).

190   We then summarize all earthquake magnitudes in our model results. In general, most
191 ruptures initiated in high locking regions (locking degree > 0.75) will develop into earthquakes
192 with $M_W \geq 7.2$ in the Nicoya region (Figure 3). However, ruptures started from the moderate
193 locking region (0.5 < locking degree < 0.75) form smaller earthquakes with M_W 5 to 6. Such
194 trend does not change with the different nucleation sizes (Figure 3d), although at the same

location the earthquake magnitude increases with the nucleation size. One striking feature is that we do not observe any earthquakes with magnitudes between 6 and 7 (Figure 3d).

We performed the same analysis for the Feng locking model, and found that despite difference in the spatial distribution of locking degrees and the resultant rupture scenarios, the hypocentre-dependent magnitudes are still observed (Figure 4). In regions with locking degree greater than 0.55, less than 50% of nucleation zones could generate Mw>7 earthquakes (Figure 4). Similarly, we do not observe earthquakes with magnitudes of 6 to 7, indicating that the magnitudes of earthquakes are controlled by heterogeneous stress levels on the megathrust if the strength is uniform.

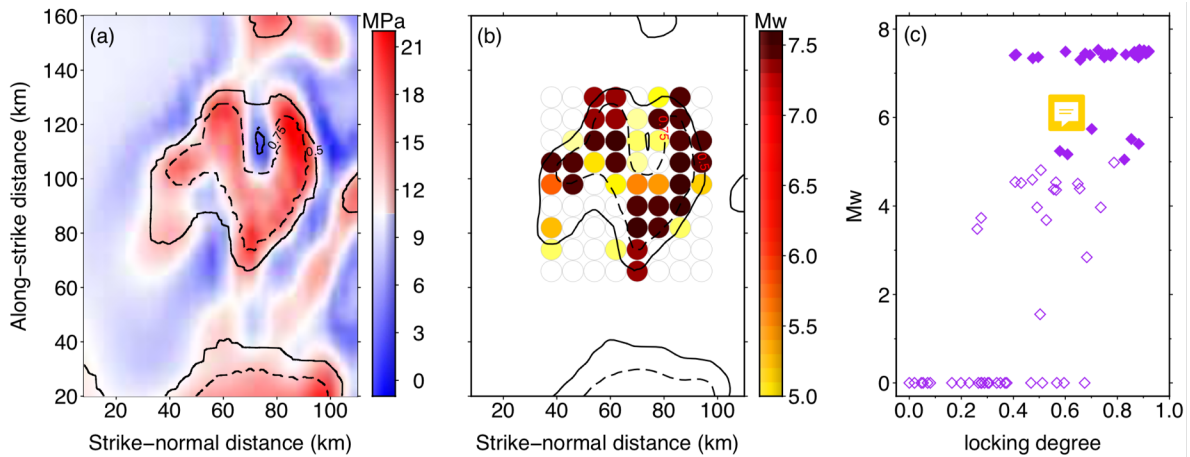**Figure 4:** Same with Figure 3, except for the Feng locking model.

4. Discussion

4.1 Heterogeneous stress distribution and earthquake magnitude

Although ruptures in this study are artificially initiated, our results are not simply the consequence of nucleation processes. We ensure that stress excess in each nucleation node is identical (i.e. 0.01 MPa) so that the hypocentral dependent earthquake magnitudes are not controlled by the variation in stress excess. It is also shown in our models that nucleating ruptures at regions with nearly identical initial stresses lead to different magnitudes and scenarios (Figure 2), reflecting the dominant effects on rupture extents of the heterogeneous stress distribution. Indeed, stress field heterogeneity has been shown in a number of studies to significantly modulate rupture propagation (e.g., *Ripperger et al.*, 2007; *Yang et al.*, 2012; *Yang et al.*, 2013; *Weng et al.*, 2015).

The hypocentral dependence of magnitudes is a result of the "effective" seismogenic zone induced by the variation in difference between the initial stress and yield strength (uniform in this study) on the fault. As shown in a recent numerical experiment considering finite downdip seismogenic width (*Weng and Yang*, 2017), ruptures may spontaneously stop without additional structural or stress barriers on a fault with a small seismogenic width. These ruptures are termed self-arresting ruptures, which are caused by the insufficient rupture kinetic energy that is needed to overcome the fracture energy on the fault so that the rupture may continue propagating. In comparison, a fault having large seismogenic width can host large earthquakes because ruptures can spontaneously propagate and break the entire seismogenic zone (*Weng and Yang*, 2017), termed breakaway ruptures. In our models, these M7+ earthquake scenarios break at least one highly locked patch because the rupture started in relatively large "effective" seismogenic region and then propagated much further. Otherwise, they may just form smaller magnitude events (Figure 3&4) due to the limited "effective" seismogenic zone bounded by heterogeneous stress distribution.

230   In our model, the heterogeneous stress results from the spatial variation in locking where
231 larger gradients lead to higher stress (*Yin et al.*, 2016; *Yin et al.*, 2017; *Weng and Yang*, 2018).
232 In both locking models (*Feng et al.*, 2012; *Xue et al.*, 2015), the grid size on the megathrust is
233 5 km and the resolution is more than 20 km so that strong variations in a small spatial scale
234 may not be captured. Again, the same caveat about considering only the relative nature of these
235 results is because they are derived from subjectively smoothed locking models. The faults are
236 likely much more heterogeneous, forming smaller asperities that cannot be easily observed
237 with surface geodetic techniques. If such small asperities rupture, we should then observe a
238 large number of moderate interface earthquakes, which is however not the case in the Nicoya
239 region (Figure 1). From 1976 to September 2012, we only find 7 earthquakes with Mw 5+ from
240 the GCMT catalog that had thrust mechanisms (Figure 1). Five out of the seven events are
241 located in the locking region, while others are outside (Figure 1a). For ~82 mm/yr of
242 convergence (*DeMets et al.*, 2010), the lack of more frequent moderate earthquakes implies
243 strong locking with limited small-scale heterogeneities, which were perhaps caused by seafloor
244 roughness as is immediately to the south (*Bilek et al.* 2003). The magnitude gap (M6-7) in our
245 numerical results, irrespective of the input locking models, is consistent with observations
246 beneath Nicoya prior to the 2012 mainshock, in which earthquakes with magnitudes between
247 5.5 and 7 are very rare (Figure 1c). Even if we consider the time window after the mainshock,
248 the magnitudes of most aftershocks do not exceed 5.5 (*Chaves et al.*, 2017). Thus the magnitude
249 gap may reflect to some extents the spatial heterogeneity of stress and locking in the Nicoya
250 region.
251   In contrast, there are a number of shallow thrust earthquakes with magnitudes 5-6+ in the
252 region northwest to the locked patches (Figure 1), indicating abundant small asperities. High-
253 resolution locking models based on geodetic data are not available due to the lack of constraint
254 on the shallow megathrust. But this portion is likely creeping, and the creeping is associated
255 with numerous normal faulting fabrics and potentially subducted seamounts (*Wang and Bilek*,
256 2013).

4.2 Implications on earthquake and tsunami hazard assessment

258   In addition to estimating the locations and sizes of potential earthquakes, practical
259 seismic assessments should also forecast local ground shaking to evaluate hazard and mitigate
260 risk. Our results show that, although two earthquake scenarios initiating from high locking
261 regions may have the same magnitude in the Nicoya peninsula, the ground motion could be
262 drastically different due to rupture directivity. To exemplify this, we nucleated two earthquakes
263 with similar magnitudes (i.e. 7.42 and 7.49) from the Feng locking model, while one initiated
264 from offshore and the other one nucleated inland (Figure 5). For the two cases, the ruptures
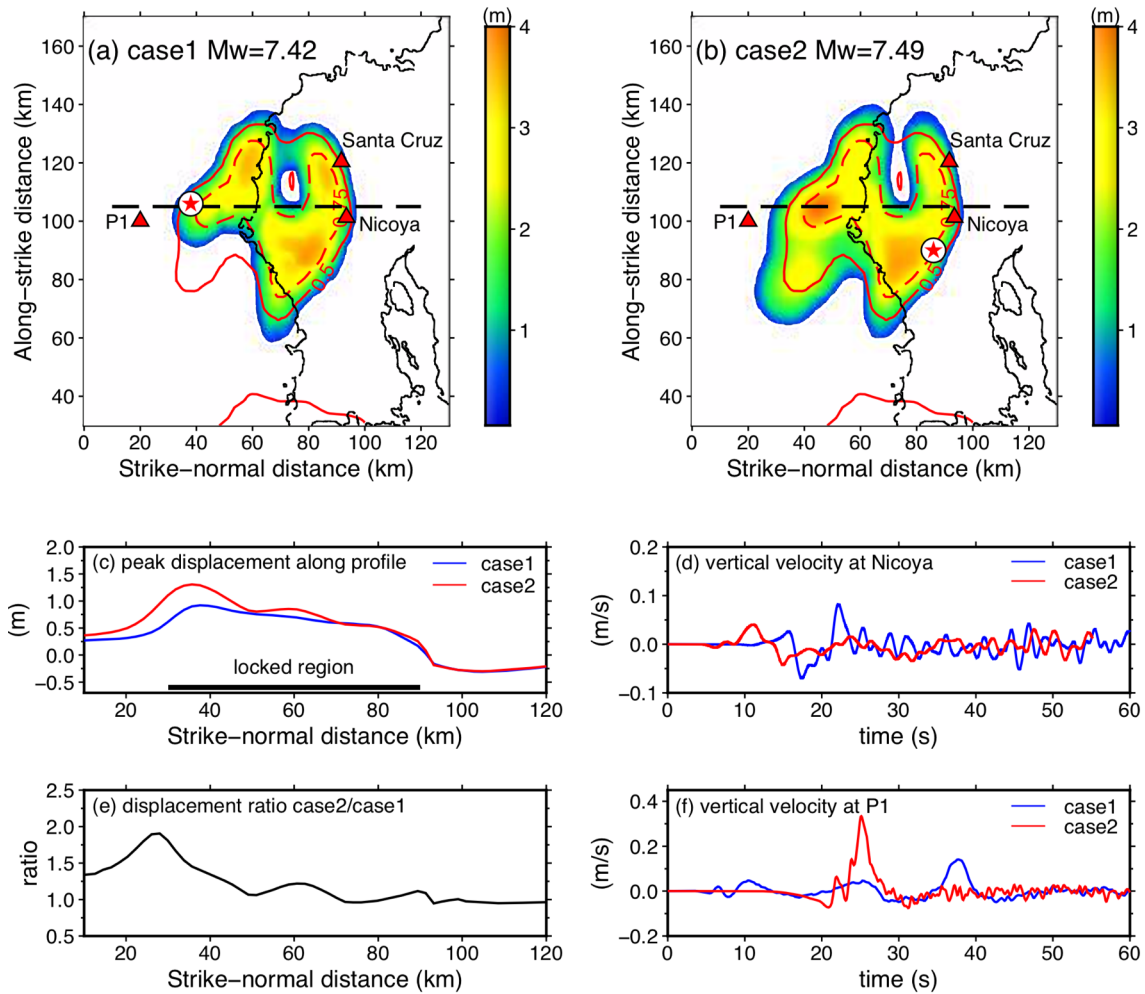265 break both offshore and beneath land, resulting in similar final slip distribution (Figure 5 a&b).

Figure 5: Final slip distribution of rupture scenarios nucleated at two different locations, offshore (a) and inland (b), using the Feng locking model (contours) with nucleation sizes of 4 km. Dash lines show a profile to compare ground displacements. Triangles denote hypothetical stations, one offshore (P1) and two at towns of Nicoya and Santa Cruz. Peak displacements (c) and final slip distribution (e) along the profile from the two rupture scenarios. Vertical velocities recorded at Nicoya (d) and P1 (f) from the two scenarios, respectively.

When the rupture initiated from inland (Figure 5b), the up-dip propagating rupture would lead to much higher ground velocity offshore, as shown in the record of a hypothetical station at P1 (Figure 5f); while the down-dip rupture will produce nearly as twice as large of peak-to-peak vertical velocity at the town of Nicoya (Figure 5d), despite that the town is much closer to the epicentre of up-dip case rupture (Figure 5b).

In addition to playing roles in ground shaking, the rupture directivity affects shallow slip distribution and potential tsunami generation. For the rupture nucleated offshore (Figure 5a), the peak ground displacements along a profile (i.e. along-strike distance equals to 105km) show uplift of the ruptured area, with the maximum displacement of ~0.9 m near the epicentre (Figure 5c). In contrast, the rupture nucleated from below land, and propagating up-dip, would lead to larger shallow slip (Figure 5e) and ground displacements (Figure 5c) along the profile than in the prior scenario, due to the rupture directivity. In the offshore region, the ground displacement could be amplified nearly twice (Figure 5c), and such up-dip environment is more prone to tsunami excitation.

We then summarize the slip distributions for all rupture scenarios nucleating from different hypocentres that have nearly identical moment magnitudes (>7.4). For ruptures initiating from shallow depths (i.e. <18 km) in the Nicoya region (Figure 6a), the downdip slip

amplitudes are similar with those nucleating from greater depths (Figure 6b). In addition, the
amplitudes and depths of peak slip show quite good consistency in the deeper part with those
during the 2012 Nicoya earthquake, which nucleated from offshore (*Yue et al.*, 2013). In
contrast, the slip at shallow depths (< 15 km) resulting from deeper hypocentres are obviously
larger than those nucleating at shallow depths (Figure 6b). Such systematically larger shallow
slips from deeper nucleation points will lead to larger ground displacements offshore, which in
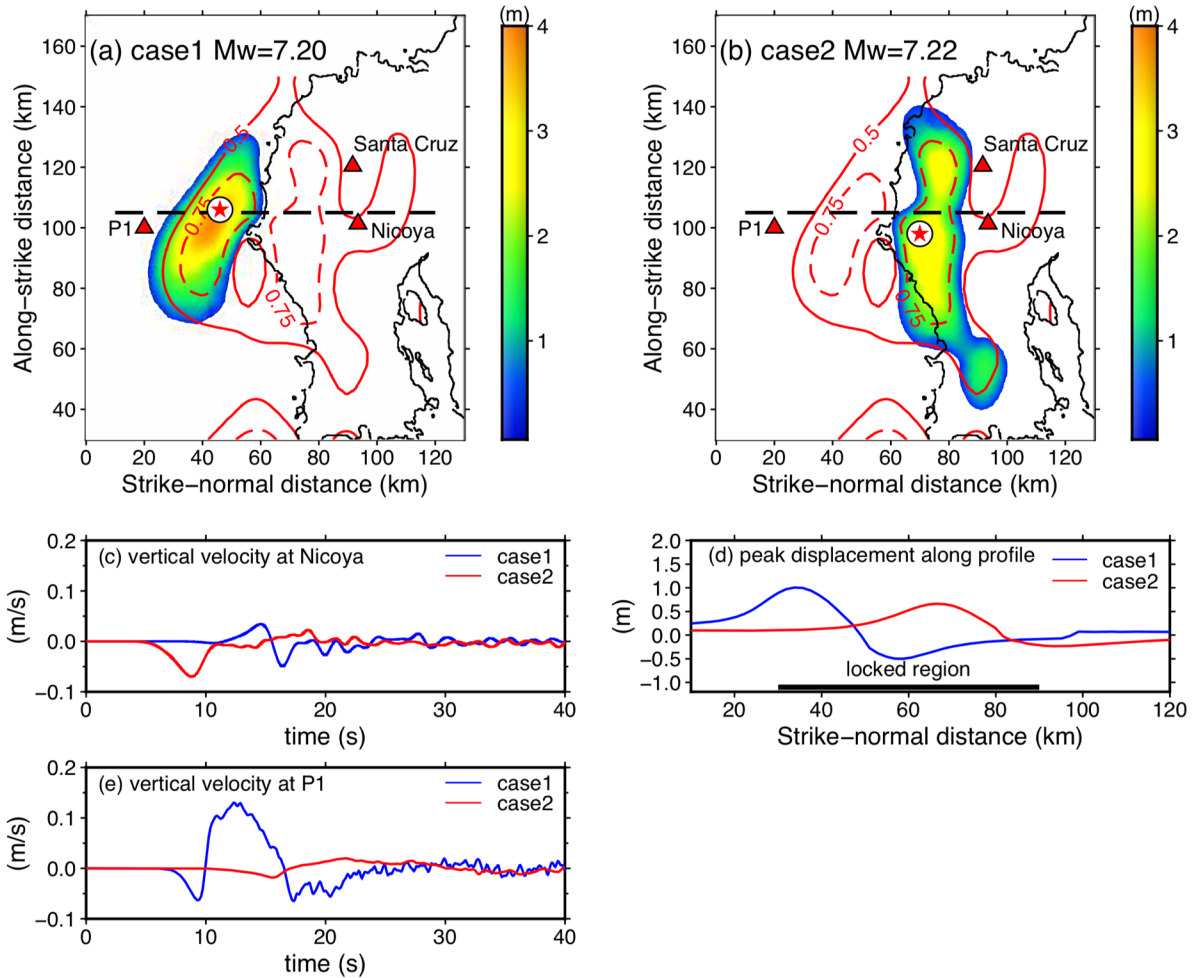turn increase the tsunamic-genetic potential.

Figure 6: (a) Updip (light blue) and downdip (red) nucleation locations with nearly identical final moment
magnitudes (Mw>7.4) of rupture scenarios. Contours show the locking distribution. (b) Slip distributions from
all rupture scenarios along a profile (red dash line) shown in panel (a). Red and blue lines show the average
values, and the shaded areas indicate the 1-σ confidence. Black dashed line is from Yue's kinematic source
model (*Yue et al.*, 2013).

Interestingly, the M_W 7.7 1950 Nicoya earthquake, while centered similarly below the
peninsula, did create a meter-level tsunami across portions of the southern peninsula, and up
to 10 cm inside the Gulf of Nicoya, despite having 12 years less to rebuild since its last major
event in 1900 (*Protti et al.*, 2001). Perhaps the major difference between the 1950 and 2012
events are not the prior locking, but where nucleation initiated, the 1950 event initiating down-
dip (*Guendel*, 1986), and the 2012 earthquake initiating up-dip (*Yue et al.*, 2013).

Megathrust earthquakes may generate tsunami by causing significant vertical seafloor
displacement or less commonly by generating submarine landslides. As shown above, based
on Feng's locking model, the rupture that nucleated from the high-locking region generated
substantially larger ground displacements on the seafloor due to up-dip rupture directivity
(Figure 5), and may lead to tsunami generation. If we can produce a large number of ground

motion database for each rupture scenario at different hypocentres with a reliable locking model, then the seafloor ground movements can lead to tsunami wave height prediction along the coast by conducting numerical simulation of tsunami waves, given appropriate bathymetric information. In the most optimistic case, an earthquake hypocentre can be automatically determined with high-resolution by local seismic network, and can then be directly used to predict potential tsunami wave heights from the precomputed database from one of the determined scenario runs. A more realistic approach would be to include a probability-distribution function of scenario inundations for a given hypocentre and an estimation of error in its location. Because tsunami waves propagate much slower than seismic waves, such approach would be effective for near-field earthquake-induced tsunami early-warning.

5. Conclusions

In this study, we quantitatively evaluate potential earthquake sizes and rupture scenarios from interseismic locking models and demonstrate that the initiation point of the rupture plays critical roles in controlling the earthquake sizes due to the heterogeneous stress distribution. Our results show that ruptures initiating from high locking zones more likely grow into larger earthquakes, with 40% becoming M>7.2 in Nicoya peninsula. Irrespective of the input locking models we do not find scenario ruptures that have magnitudes of 6-7, which is largely consistent with observations and probably reflects to some extents the degree of stress heterogeneity in the Nicoya peninsula. Furthermore, the rupture directivity effects are critical in ground shaking and displacement prediction given the same earthquake magnitude, shedding lights on near-field tsunami early warning. The results of hypocentre-dependent earthquake magnitudes in a given interseismic locking distribution pose challenges, yet the numerically derived rupture scenarios can be used for evaluating earthquake and tsunami hazard.

Data availability: All results in this study are generated from numerical simulations and can be requested by contacting the corresponding author.

Reference:
1. Aagaard, B. T., Knepley, M. G., Williams, C. A., 2013. A domain decomposition approach to implementing fault slip in finite-element models of quasi-static and dynamic crustal deformation. *J. Geophys. Res.* **118,** 3059-1079.
2. Audet, P., Schwartz, S. Y., 2013. Hydrologic control of forearc strength and seismicity in the Costa Rican subduction zone. *Nat. Geosci.* **6(10)**, 852-855.
3. Bilek, S. L., S. Y. Schwartz, and H. R. DeShon (2003), Control of seafloor roughness on earthquake rupture behavior, *Geology*, *31*(5), 455–5, doi:10.1130/0091-7613(2003)031.
4. Bizzarri, A., 2010. How to promote earthquake ruptures: Different nucleation strategies in a dynamic model with slip-weakening friction. *Bull. Seismol. Soc. Am.* **100**, 923–940.
5. Burgette, R. J., Weldon, R. J., Schmidt, D. A., 2009. Interseismic uplift rates for western Oregon and along-strike variation in locking on the Cascadia subduction zone. *J. Geophys. Res.* **114**, B01408.

6. Chaves, E. J., and S. Y. Schwartz, 2016, Monitoring transient changes within overpressured regions of subduction zones using ambient seismic noise, *Sci. Adv.*, 2:e1501289

7. Chaves, E. J., L. Duboeuf, S. Y. Schwartz, T. Lay, and J. Kintner, 2017, Aftershocks of the 2012 Mw 7.6 Nicoya, Costa Rica, earthquake and mechanics of the plate interface, *Bull. Seismol. Soc. Am.*, 107(3), 1227-1239, doi: 10.1785/0120160283

8. DeMets, C., Gordon, R. G., & Argus, D. F., 2010. Geologically current plate motions. *Geophysical Journal International, 181*(1), 1-80.

9. Dixon, T. H., Jiang, Y., Malservisi, R., McCaffrey, R., Voss, N., Protti, M., Gonzalez, V., 2014. Earthquake and tsunami forecasts: Relation of slow slip events to subsequent earthquake rupture. *Proc. Natl. Acad. Sci. U.S.A.* **111(48)**, 17039-17044.

10. Feng, L., Newman, A. V., Protti, M., Gonzalez, V., Jiang, Y., Dixon, T. H., 2012. Active deformation near the Nicoya Peninsula, northwestern Costa Rica, between 1996 and 2010: Interseismic megathrust coupling. *J. Geophys. Res. Solid Earth* **117,** B06407.

11. Guendel, F., 1986. Seismotectonics of Costa Rica: An analytical view of the southern terminus of the Middle America Trench. Ph.D. thesis, 157 pp., Univ. of Calif., Santa Cruz.

12. Harris, R. N., Spinelli, G., Ranero, C. R., Grevemeyer, I., Villinger, H., Barckhausen, U., 2010. Thermal regime of the Costa Rican convergent margin: 2. Thermal models of the shallow Middle America subduction zone offshore Costa Rica. *Geochem. Geophys. Geosyst.* **11**, Q12S29.

13. Hok, S., Fukuyama, E., Hashimoto, C., 2011. Dynamic rupture scenarios of anticipated Nankai-Tonankai earthquakes, southwest Japan. *J. Geophys. Res.* **116***,* B12319.

14. Hori, T., Kato, N., Hirahara, K., Baba, T., Kaneda, Y., 2004. A numerical simulation of earthquake cycles along the Nankai Trough in southwest Japan: lateral variation in frictional property due to the slab geometry controls the nucleation position. *Earth Planet. Sci. Lett.* **228(3)**, 215-226.

15. Ida, Y., 1972. Cohesive force across the tip of a longitudinal-shear crack and Griffith's specific surface energy. *J. Geophys. Res.* **77(20)**, 3796-3805.

16. Kyriakopoulos, C., Newman, A. V., A. M. Thomas, M. Moore-Driskell, and G. T. Farmer 2015, A new seismically constrained subduction interface model for Central America, *J. Geophys. Res.*, 120(8), 5535-5548

17. Kyriakopoulos, C., Newman, A. V., 2016. Structural asperity focusing locking and earthquake slip along the Nicoya megathrust, Costa Rica. *J. Geophys. Res. Solid Earth* **121(7)**, 5461-5476.

18. Lapusta, N., Rice, J. R., 2003. Nucleation and early seismic propagation of small and large events in a crustal earthquake model. *J. Geophys. Res. Solid Earth* **108(B4),** B000793.

19. Li, S., Wang, K., Wang, Y., Jiang, Y., Dosso, S. E., 2018, Geodetically inferred locking state of the Cascadia megathrust based on a viscoelastic Earth model. *J. Geophys. Res.: Solid Earth*, 123. doi：10.1029/2018JB015620.

20. McCaffrey, R., King, R. W., Payne, S. J., Lancaster, M., 2013. Active tectonics of northwestern US inferred from GPS-derived surface velocities. *J. Geophys. Res. Solid Earth* **118(2)**, 709-723.

21. Moreno, M., Rosenau, M., Oncken, O., 2010. 2010 Maule earthquake slip correlates with pre-seismic locking of Andean subduction zone. *Nature* **467(7312)**, 198-202.

22. Pollitz, F.F., Evans, E.L., 2017. Implications of the earthquake cycle for inferring fault locking on the Cascadia megathrust. *Geophys. J. Int.*, 209, 167–185, doi: 10.1093/gji/ggx009.

23. Protti, M., 2001. Significance of an earthquake early warning system for vulnerable essential facilities: The example of a potential implementation in Costa Rica. *ISDR Informs*, **3**, 21-4.

24. Quintero, R., Zahradník, J., Sokos, E., 2014. Near-regional CMT and multiple-point source solution of the September 5, 2012, Nicoya, Costa Rica Mw 7.6 (GCMT) earthquake. *J. S. Am. Earth Sci.* **55**, 155-165.

25. Rice, J. R., 1992. Fault stress state, pore pressure distributions, and the weakness of San Andreas Fault. In Fault mechanics and transport properties of rocks (pp. 475-503). San Diego, CA: Academic Press.

26. Ripperger, J., Ampuero, J.‐P., Mai, P. M., Giardini, D., 2007. Earthquake source characteristics from dynamic rupture with constrained stochastic fault stress. *J. Geophys. Res.*, **112**, B04311.

27. Saffer, D. M., Tobin, H. J., 2011. Hydrogeology and mechanics of subduction forearcs: Fluid flow and pore pressure. *Annu. Rev. Earth Planet. Sci. 2011* **39:1**, 157-186.

28. Schmalzle, G. M., McCaffrey, R., Creager, K. C., 2014. Central Cascadia subduction zone creep. *Geochem. Geophys. Geosyst.*, 15, 1515–1532, doi: 10.1002/2013GC005172.

29. Wang, K., Hu, Y., He, J., 2012. Deformation cycles of subduction earthquakes in a viscoelastic Earth. *Nature 484*(7394), 327-332.

30. Wang K, Bilek SL. 2014. Fault creep caused by subduction of rough seafloor relief. *Tectonophys.,* 610:1–24

31. Weng, H., Huang, J., Yang, H., 2015. Barrier-induced supershear ruptures on a slip-weakening fault. *Geophys. Res. Lett.*, **42(12)**, 4824-4832.

32. Weng, H., Yang, H., 2017. Seismogenic width controls aspect ratios of earthquake ruptures. *Geophys. Res. Lett.*, **44(6)***,* 2725-2732.

33. Weng, H., Yang, H., 2018. Constraining frictional properties on fault by dynamic rupture simulations and near-field observations. *J. Geophys. Res.*, doi:10.1029/2017JB015414.

34. Williamson, A. L., & Newman, A. V. (2018). Limitations of the resolvability of finite-fault models using static land-based geodesy and open-ocean tsunami waveforms. *J. Geophys. Res.*, 123. https://doi.org/10.1029/2018JB016091.

35. Xue, L., Schwartz, S., Liu, Z., Feng, L., 2015. Interseismic megathrust coupling beneath Nicoya Peninsula, Costa Rica, from the joint inversion of InSAR and GPS data. *J. Geophys. Res.* **120(5)***,* 3707-3722.

36. Yang, H., Liu, Y., Lin, J., 2012. Effects of subducted seamount on megathrust earthquake nucleation and rupture propagation. *Geophys. Res. Lett.* **39**, L24302.

37. Yang, H., Liu, Y., Lin, J., 2013. Geometrical effects of a subduction seamount on stopping megathrust rupture. *Geophys. Res. Lett.* **40(10),** 2011-2016.

38. Yang, H., S. Yao, B. He, A. Newman, and H. Weng (2019), Deriving rupture scenarios from interseismic locking distributions along the subduction megathrust, *J. Geophys. Res.* under review

39. Yao, S., and Yang, H. (2018). Determination of coseismic frictional properties on the megathrust during the 2012 M7.6 Nicoya earthquake, *AGU Fall Meeting*, T41H-0407

40. Yin, J., Yang, H., Yao, H., Weng, H., 2016. Coseismic radiation and stress drop during the 2015 Mw 8.3 Illapel, Chile megathrust earthquake. *Geophys. Res. Lett.* **43**, 1520–1528.

41. Yin, J., Yao, H., Yang, H, Liu, J., Qin, W., Zhang, H., 2017. Frequency-dependent rupture process, stress change, and Seismogenic mechanism of the 25 April 2015 Nepal Gorkha Mw 7.8 earthquake. *Science China Earth Sciences*, 60(4),796-808.

448   42. Yue, H., Lay, T., Schwartz, S. Y., Rivera, L., Protti, M., Dixon, T. H., Owen, S.,
449   Newman, A. V., 2013. The 5 September 2012 Nicoya, Costa Rica Mw 7.6 earthquake
450   rupture process from joint inversion of high-rate GPS, strong-motion, and teleseismic
451   P wave data and its relationship to adjacent plate boundary interface properties. *J.*
452   *Geophys. Res. Solid Earth* **118(10)**, 5453-5466.